

TSAR-MVS: Textureless-aware Segmentation and Correlative Refinement Guided Multi-View Stereo

Zhenlong Yuan¹, Jiakai Cao¹, Hao Jiang¹, Zhaoqi Wang¹, and Zhaoxin Li^{✉1}

¹Institute of Computing Technology, Chinese Academy of Sciences, Beijing, China

Abstract—The reconstruction of textureless areas has long been a challenging problem in MVS due to lack of reliable pixel correspondences between images. In this paper, we propose the Textureless-aware Segmentation And Correlative Refinement guided Multi-View Stereo (TSAR-MVS), a novel method that effectively tackles challenges posed by textureless areas in 3D reconstruction through filtering, refinement and segmentation. First, we implement joint hypothesis filtering, a technique that merges a confidence estimator with a disparity discontinuity detector to eliminate incorrect depth estimations. Second, to spread the pixels with confident depth, we introduce an iterative correlation refinement strategy that leverages RANSAC to generate superpixels, succeeded by a median filter for broadening the influence of accurately determined pixels. Finally, we present a textureless-aware segmentation method that leverages edge detection and line detection for accurately identify large textureless regions to be fitted using 3D planes. Experiments on extensive datasets demonstrate that our method significantly outperforms most non-learning methods and exhibits robustness to textureless areas while preserving fine details.

Index Terms—Multi-View Stereo, 3D reconstruction, Filtering, Superpixel, Segmentation.

I. INTRODUCTION

MULTI-view Stereo (MVS) aims to rebuild dense 3D scenes or objects from a series of calibrated RGB images. It has a broad range of applications in fields such as virtual reality, 3D printing, and autonomous driving, leading to numerous efficient MVS frameworks [1], [2], [3], [4], [5]. Nonetheless, despite the accuracy has been rapidly improved by the latest methods [6], [7], these techniques frequently face challenges when dealing with textureless areas.

Recently, PatchMatch Stereo based-methods [8], [9], [10] have accomplished remarkable successes in reconstructing dense 3D models from large-scale imagery. These methods typically follow an organized pipeline including initialization, propagation and refinement, positioning them uniquely suited for reconstructing scenes with unstructured viewpoints. However, due to the unreliable photometric consistency, state-of-the-art methods [11], [12], [13], [14] still perform poorly when facing with large area of textureless regions.

Zhenlong Yuan, Jiakai Cao, Hao Jiang and Zhaoqi Wang are with Institute of Computing Technology, Chinese Academy of Sciences, Beijing 100190, China (e-mail: yuanzhenlong21b@ict.ac.cn; caojiakai21@mails.ucas.ac.cn; jianghao@ict.ac.cn; zqwang@ict.ac.cn)

Zhaoxin Li is with Agricultural Information Institute, Chinese Academy of Agricultural Sciences, Beijing 100081, China and Key Laboratory of Agricultural Big Data, Ministry of Agriculture and Rural Affairs, Beijing 100081, China (e-mail: cszli@hotmail.com)

Corresponding author: Zhaoxin Li (cszli@hotmail.com)

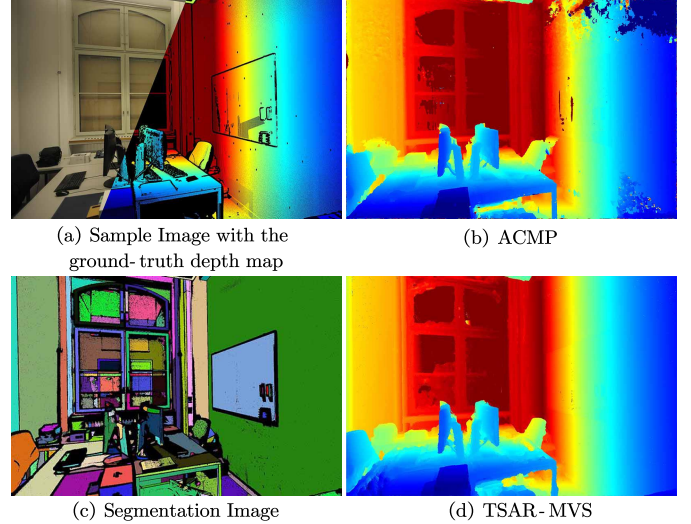


Fig. 1. An instance of depth reconstruction on ETH3D dataset. ACMP [12] (b) yields inferior reconstruction results owing to a significant amount of textureless surfaces. The proposed textureless-aware segmentation (c) provides guidance for TSAR-MVS (d) to distinguish and planarize textureless areas.

Ambiguity in matching corresponding points between images often arises within enormous textureless regions like walls and floors, which lack discriminative features, thus resulting in unsuccessful reconstruction. Despite several approaches attempt to mitigate this issue, most contemporary MVS methods fail to yield satisfactory results.

Some traditional methods [11], [12], [15] leverage multi-scale geometric consistency and triangulated planar prior to address this challenge. Through obtaining planar hypotheses at coarser scales and propagating reliable ones into finer scales, these methods manage to effectively reconstruct a portion of textureless areas. Yet, the integration of larger textureless areas remains problematic due to their limited patch sizes. One line of approaches [16], [13], [10] attempt to utilize superpixels and the RANSAC algorithm to alleviate the problem. However, constraints such as a fixed threshold and strict assumption of data distribution results in poor planarization for certain superpixels. APD-MVS [17] utilizes adaptive deformable patch with cascade architecture. Nevertheless, its excessive PatchMatch iterations often lead the process time-consuming, making it impractical for application on large-scale datasets like ETH3D.

Some learning-based methods, such as [18], [7] leverage a coarse-to-fine cascading architecture to address the issue of textureless areas. By refining and upsampling depth maps

from low resolution, these methods can effectively expand the receptive field while decreasing the cost volumes. However, these methods typically require substantial memory and time consumption. To circumvent this, several methods like [14], [19] attempt to employ lightweight gated recurrent units (GRU) to encode the depth probability distribution for each pixel. However, since GRU is primarily used to capture sequential information, their capacity for spatial recognition becomes constrained. Consequently, they often exhibit limitation in reconstructing untextured areas where feature information is elusive. Other methods, like [20], [21] introduce an epipolar module to assemble high-resolution images into limited-size cost volumes. However, they often exhibit limited generalization, inhibiting their application in reconstructing scenarios with diverse characteristics.

In an effort to circumvent the aforementioned challenges, we propose Textureless-aware Segmentation And Correlative Refinement guided Multi-View Stereo (TSAR-MVS), a novel method that specifically designed to reconstruct textureless areas. Our method assumes that man-made scenes usually contain a large number of planar structures. We attempt to segment the pixels in textureless regions and adopt plane fitting technology to reassign the high-quality depth values by using a set of pixels with high confidence. Specifically, we first introduce a joint hypothesis filter consisting of a confidence estimator and a disparity discontinuity detector to provisionally remove outliers. Inspired by [22], [23], we adopt matching cost and adapted Left-Right Consistency (LRC) as the confidence to filter the wrong estimates. Furthermore, we maintain the object edges in the depth map, underpinning the assumption [24] that disparity should be continuous. With this, we can treat small disparity discontinuities as outliers that need to be removed, while preserving the object edges which are shown as large discontinuities in disparity.

Subsequently, to propagate the confident pixels with correct depth, we propose an iterative correlation refinement procedure. In each iteration, we first cluster pixels with similar perceptual features into various superpixels, then we apply RANSAC to planarize each superpixel, resulting in pixels within a superpixel sharing a consistent depth. For each superpixel, an adaptive threshold is set according to their data distribution and the number of pixels. Following this, a pixel-wise weighted median filtering (WMF) is used to propagate the correct depth to the surrounding areas. This iterative process is conducted over several rounds for the propagation of reliable depth. Finally, another WMF is applied for the interpolation of depth and normal of the remaining pixels.

Additionally, we propose a textureless-aware segmentation method that combines edge detection and line detection. Typically, in man-made scenarios [25], [26], pixels within the same textureless areas exhibit a high degree of similarity. Thus, we can separate textureless areas and independently estimate the depth of their homogeneous surfaces. Specifically, we apply the Roberts edge detection to extract high-frequency information, followed by the Hough line detection that enhances region discrimination by concatenating separated edges into lines. By aggregating residual pixels into miscellaneous areas, we can distinguish textureless areas and further planarize them,

improving the precision of our 3D reconstruction approach.

Experiments on extensive datasets, including the ETH3D high-resolution multi-view benchmark and the Strecha dataset, demonstrate that our method significantly outperforms other MVS methods. It exhibits robustness to recovery textureless areas of varying sizes. Furthermore, We prove that our method can be incorporated as a component into other reconstruction pipelines and improve the performance.

In summary, our contributions are as follows:

- 1) We propose a novel joint hypothesis filter by adeptly merging a confidence estimator and disparity discontinuities to yield an aggregation score that effectively eliminate outliers.
- 2) We present an iterative correlation refinement procedure that iteratively employs RANSAC and WMF to refine pixel estimates based on the surrounding confident neighbors.
- 3) We introduce a textureless-aware segmentation technique that merges edge and line detection, thereby enhancing distinction and planarization of textureless areas.
- 4) Through extensive experiments, we verified that our method can achieve better reconstruction than other methods.

II. RELATED WORK

Conventional MVS methods can be categorized into four types, voxel based approaches [27], [28], deformable polygonal meshes based approaches [29], [30], patch based approaches [31], [32] and depth maps based approaches [33], [34]. Voxel based approaches enclose the scene with a bounding box and divide it into voxel grids. Polygonal meshes based approaches rely on a trusted initialization guess to iteratively improve accuracy. Patch based approaches deem the scene to be small patches, which commonly demand postprocessing. Depth map based approaches progressively estimate corresponding depth maps and requires fusion for point cloud generation. Here we only review related depth maps based approaches and discuss methods concerned with PatchMatch Multi-View Stereo and Superpixel.

Deep-learning based MVS methods [35], [21], [20], [36], [37] that train learnable cost volumes and 3D regularization for reconstruction have also been proposed. Yao et al. [6], [38] introduced a novel architecture featuring learnable cost volume through 3D regularization strategy and further regularize cost along the depth direction via the gated recurrent unit (GRU). Gu et al. [18] further proposed a cascaded refinement framework with coarse-to-fine strategy to enhance robustness of reconstruction. Xu and Tao [39] designed a visibility network for prediction of neighboring images and an anti-noise training strategy for disturbing views. However, their growing complexity of network architectures require a large amount of training data and are prone to degradation on target domains that are distributed differently from the training set.

A. PatchMatch Multi-View Stereo

Barnes et al. [40] proposed the crucial theory of PatchMatch by random initialization and propagation to cooperatively search approximate image patches pairs. Bleyer et al. [41] first proposed the PatchMatch Stereo that estimates 3D planes for

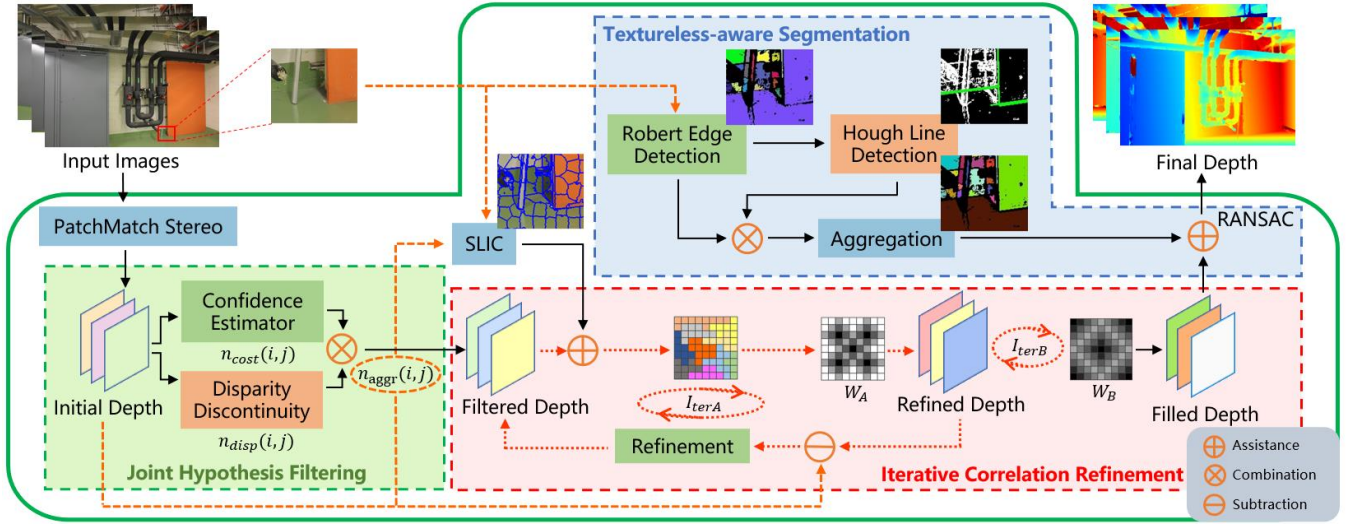


Fig. 2. An illustrated pipeline of our proposed method. We first acquire initial depth maps through a baseline PatchMatch Stereo method with adaptive checkerboard propagation. Then the joint hypothesis filtering merges a confidence estimator with a disparity discontinuity detector to eliminate incorrect depth estimations. Next, the proposed iterative correlation refinement enhances the reliability of pixel estimates through two distinct iteration procedure. The first iteration I_{iterA} is conducted by repeatedly integrating RANSAC and WMF W_A on a superpixel basis for pixel renewal. Subsequently iteration I_{iterB} is executed by consistently adopting another WMF W_B for the interpolation of the remaining unreliable pixels. Furthermore, a textureless-aware segmentation is utilized for planarization of textureless areas. By integrating Robert edge detection and Hough line detection, we identify large textureless areas for planarization and yield the final depths.

each pixels in disparity domain, and extended the spatial propagation to both view and time propagation. Subsequently, Galliani et al. [42] optimized sequential propagation scheme into a checkerboard diffusion like propagation scheme. Schönberger et al. [34] further achieved concurrently depth refinement and 3D fusion by jointly predicting depths and normals.

Additionally, Xu and Tao [11] developed multi-hypothesis view selection for cost aggregation and attempted to restore textureless areas through multi-scale scheme. They To address weak textures, Xu and Tao [12], [15] further introduced planar prior PatchMatch supported by a probabilistic graphical model to optimize cost aggregation. Moreover, Wang et al. [14] integrated PatchMatch into network and employed a learnable adaptive module for adaptive cost computation. Yet limited by window size, above methods are still not ideal in estimating textureless areas, nor can they adequately leverage relevance between neighbors to dislodge erroneous estimates.

B. Superpixel

Gouveia et al. [43] adopted superpixel-based partition for planarization and introduced the random forest for filtering. Furthermore, Zhang et al. [16] classified images into superpixels and then formulated a two-layer Markov Random Field for alignment. Romanoni et al. [13] employed SEED within two scales and introduced texture coefficient for different assignments. Kuhn et al. [10] further achieved aggregation of textureless areas with a region-growing superpixel approach.

Recently, Xue et al. [44] employed a Markov Random Field (MRF) founded on superpixels to compatibly simulate the correlation between edge depth and superpixel depth. Jung and Han [45] overcome the occlusion in 3D reconstruction by projecting superpixels onto adjacent viewpoints and performing extrapolation along a plane model. Additionally, Huang

et al. [46] integrated the mean-shift clustering approach with superpixels to generate plane priors for textureless planar regions without using semantic information. Whereas most approaches heavily depend on superpixels size or classifying situation. Besides, directly assigning pixels with their estimated superpixel planes may cause detail distortion.

III. OVERVIEW

Given a set of input observed images $\mathcal{I} = \{I_i \mid i = 1 \dots N\}$ and the corresponding camera parameters $\mathcal{P} = \{P_i \mid i = 1 \dots N\}$, our method targets on predicting their depth maps $\mathcal{D} = \{D_i \mid i = 1 \dots N\}$. Each input image is used as a reference image I_{ref} in turn, treating the remaining images as source images $I_{src} = \{I_j \mid I_j \in \mathcal{I} \wedge I_j \neq I_i\}$.

The overview of our method is graphically represented in Fig. 2. We initiate the reconstruction procedure by using a baseline PatchMatch Stereo with adaptive checkerboard propagation [11] to estimate initial depth maps for each image, which adopts the bilateral weighted adaptation of normalized cross-correlation [34] to compute the photometric cost. Subsequently, we deploy a joint hypothesis filter by fusing a confidence estimator with discontinuous disparity to construct aggregated score, thereby eliminating erroneous estimates.

Subsequently, we further apply an iterative correlation refinement to enhance the reliability of pixel estimates via a dual-phase iterative procedure. The premier iteration is performed by repeatedly applying RANSAC-based planarization and WMF on a superpixel basis to retain more reliable pixels. Then for the remaining pixels that have not been updated, we constantly leverage another WMF to assign their depths and normals from neighboring pixels in the subsequent iteration.

Finally, we introduce a textureless-aware segmentation to planarize large textureless areas. We utilize Roberts edge de-

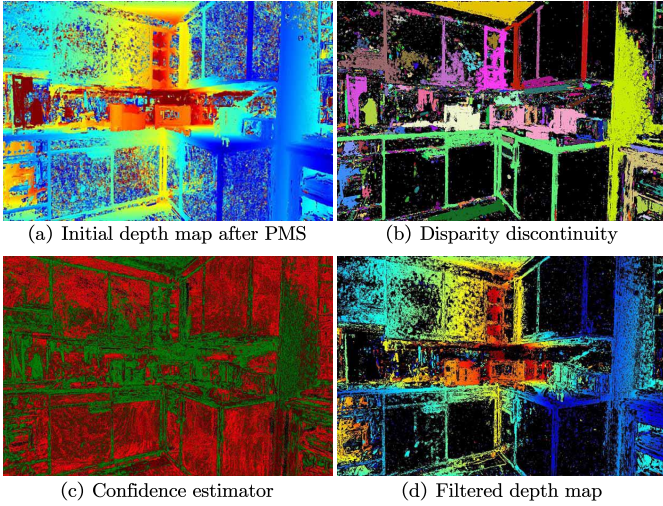


Fig. 3. Joint hypothesis filtering. Pixels associated by adjacent disparity in (b) are connected and visualized using the same color. Pixels satisfying $n_{cost}(i, j) > 1$ in (c) are denoted in green, whereas their counterparts are denoted in red for visualization. In comparison to initial depth map (a), the fused depth map (d) that merges disparity discontinuity (b) and confidence estimator (c) retains a notable portion of reliable depths.

tection to extract high-frequency information, then connect the subtle edges as line segments using Hough line detection. After grouping the remaining pixels into miscellaneous regions, we achieve the identification of textureless areas and then carry out RANSAC-based planarization.

IV. METHOD

A. Joint Hypothesis Filtering

In this subsection, we present the joint hypothesis filter, a key component of our method designed to eliminate outliers and discontinuous disparity peaks, thereby preparing the data for subsequent processing steps. As illustrated in Fig. 3, our method combines a confidence estimator and a disparity discontinuity filter to combine pixel-wise aggregated score, thereby effectively removing unreliable pixels. Distinct from previous methods [13], [10] that permanently discard pixels, our pipeline allows for the potential restoration of discarded pixels, thus preserving more possibilities based on the practical context of the iterative correlation refinement process.

1) *Confidence Estimator*: Inspired by [43], we determine the confidence based on three distinct features related to matching cost. Specifically, the total confidence $n_{cost}(i, j)$ is composed by three different confidence measures. Given a pixel (i, j) in the reference image I_{ref} with its corresponding pixel (i', j') in the source image I_{src} , the total confidence $n_{cost}(i, j)$ as a function of three different confidence measures is defined by:

$$n_{cost}(i, j) = 2 - \frac{1}{2}c_{min}(i, j) + \frac{c_{min}(i, j)}{c_{sec}(i, j)} - \left| c_{min}^{ref}(i, j) - c_{min}^{src}(i', j') \right| \quad (1)$$

The first part $c_{min}(i, j)$ is the minimal matching cost, since a lower cost generally indicates a higher degree of

relevance and thus a more accurate depth prediction. The second part $c_{min}(i, j)/c_{sec}(i, j)$ is the ratio between the minimal and sub-minimal costs. This part is introduced to detect errors induced by ambiguity during matching. The last part $|c_{min}^{ref}(i, j) - c_{min}^{src}(i', j')|$ is the absolute difference between the pixel with the optimal cost in the reference image and its corresponding pixel in the source image, which is often referred to as Left-Right Consistency (LRC).

2) *Disparity Discontinuity*: Isolated outliers frequently present themselves as minor peaks, whose depths or disparities markedly differing from surrounding pixels. However, utilizing a fixed depth threshold for filtering often proves inadequate to distinguish scenes with varying depth ranges. Consequently, we instead employ disparity filtering and, inspired by [24], upgrade the original 4-connected into an 8-connected grid to reduce mislabeling. Additionally, different from [34], our strategy merges multi-scale disparity maps and dynamic thresholds for superior results.

Specifically, each disparity map is downsample into k layers. In k^{th} level, pixels with disparity differences to their neighbors that are under the threshold 3×2^k are considered connected. We subsequently remove areas in each connected domain where the number of connected pixels is less than 5×2^k . The final disparity discontinuity confidence for each pixel is calculated by: $n_{disp}(i, j) = \sum_k n_k/k$, wherein n_k equals 1 if the pixel is preserved at the k^{th} level, and 0 otherwise.

3) *Aggregated Score*: By fusing the aforementioned cost-driven confidence detector and multi-scale disparity continuity, we synthesize an aggregated score via the following formula:

$$n_{aggr}(i, j) = \tau \times n_{cost}(i, j) + (1 - \tau) \times n_{disp}(i, j) \quad (2)$$

This unified score holistically evaluates credibility, incorporating both individual pixel costs and inter-pixel disparity correlations. Pixels (i, j) that satisfy $n_{aggr}(i, j) > \eta$ are characterized as confident pixels with reliable initial depth estimates. Moreover, $n_{aggr}(i, j)$ will also be leveraged in subsequent superpixel segmentation and pixel refinement.

B. Iterative Correlation Refinement

Most superpixel-based methods [16] commonly use RANSAC to planarize the pixels in the generated superpixels, considering them to have the same depth estimates. This approach has two potential drawbacks. First, simply replacing the depth estimates of the pixels with those of the superpixels can cause distortion, as superpixels tend to represent holistic views, while individual pixels contain specific details. Second, RANSAC has stringent requirements on data distribution, meaning that the filtering may cause inaccuracies in depth, leading to unsatisfactory results.

To address these issues, we introduce an iterative correlation refinement procedure as illustrated in Fig. 4, which is structured around two divergent iterative phases. In the preliminary phase, Given a initial disparity map calculated after PMS mentioned in III, we first use reliable pixels as input for planar prediction, assigning pixels with the correctly-predicted depths of their superpixels. Then we employ weighted median filtering (WMF) to propagate the correct depths to neighboring

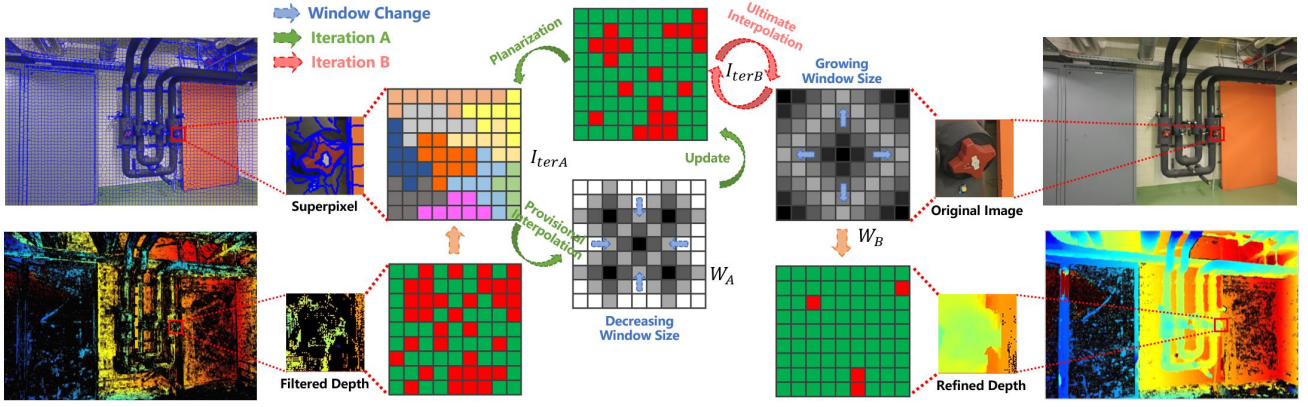


Fig. 4. Illustration of the proposed iterative correlation refinement. The framework is fundamentally structured around two discrete iterative stages, I_{terA} and I_{terB} . Given initial depth maps outputted by the baseline PatchMatch stereo, reliable pixels with green color is selected as initial input for superpixel planarization within the first stage I_{terA} . Throughout each iteration, the pixels are overlaid by the depth of planes predicted by their superpixels, and subsequently interpolated by using W_A with window size that gradually decreases according to the number of iterations. We then refine the pixels by contrasting them with the initial depth map, readying them for the next round of input. Progressing to the subsequent stage I_{terB} , we employ W_B with its window size incrementally expanding to interpolate the remaining pixels.

pixels. Following multiple iterations of this mechanism, we evaluate the disparity difference between the refined disparity dp^{est} and the initial disparity. Subsequently, in the ensuing phase, we repeatedly utilize another WMF for the interpolation of the remaining unreliable pixels.

1) *Superpixel*: The Simple Linear Iterative Clustering (SLIC) algorithm [47] is employed for image segmentation in our method, which is performed using k-means pixel clustering. However, our innovation lies in combining this with our aggregated score. Specifically, the distance between pixel p and superpixel c_k is given by:

$$D' = \sqrt{\left(\frac{d_c}{10}\right)^2 + \left(\frac{d_s}{20}\right)^2} + n_k \quad (3)$$

where d_c and d_s depict the color and spatial distance between p and c_k , n_k characterizes the mean n_{aggr} inherent to c_k . Such an integration inclines towards increasing superpixel size within textureless areas where reliable pixel distributions are more sparse, thereby facilitating their planarization.

The number of superpixels is also pivotal in achieving precise imagery. Insufficient superpixels could lead to excessive pixels being planarized together, thereby resulting in inaccuracy in depth details and loss of valuable information. Conversely, too many superpixels might pose challenges for reconstruction, as the data may be insufficient for the RANSAC algorithm to function effectively. Empirically, we opt to set the number of superpixels such that each contains approximately 400 pixels in our downsampled images.

2) *Random Sample Consensus*: We utilize RANSAC to predict 3D planes for all superpixels $\mathcal{P} = \{P_i \mid i = 1 \cdots N_{sp}\}$ in the depth range. Inspired by previous work [13], we introduce an adaptive ratio of inliers r_k^{inl} as a threshold to assess the reliability of each superpixel. This ratio is the quotient of the number of reliable pixels n_{rel}^p and the superpixel magnitude n^{sp} . However, the reliability of the plane estimate can be influenced by other factors such as the size of the superpixel, data distribution, and the chosen threshold. Therefore, solely using r_k^{inl} for depth estimation can be imprecise. To address

this, we also require the depth of the predicted 3D plane to be within an adaptive range defined by the minimum and maximum depth estimates of the pixels in the superpixel. Formally, we denote superpixel set that satisfy both parts as S , which can be defined as:

$$S \in \{P_k \mid r_k^{inl} > \sigma \wedge D_k \in [1.2 \cdot D_{min}, 0.8 \cdot D_{max}]\} \quad (4)$$

where $k \in \{1, 2, \dots, N_{sp}\}$, σ is a threshold that depends on the noise of the data, D_k is the depth of k -th superpixel, D_{min} and D_{max} respectively represent the minimum and maximum depth estimates of the pixels in the superpixel, and N_{sp} is the total number of the superpixels in the current image.

Furthermore, for better superpixel estimation, we employ an adaptive RANSAC threshold t_{ad} for each superpixel P_k , which is influenced by the depth of the center pixels D_{cen} to accommodate distinct data distributions:

$$t_{ad} = \begin{cases} D_{cen} \cdot 10^{-3} & , \text{ if } P_k \in S \\ 5 \cdot 10^{-3} & , \text{ else} \end{cases} \quad (5)$$

3) *Weighted Median Filtering*: Our method incorporates two similar weighted median filters, each with distinct objectives. The first filter is utilized in each iteration to provisionally retain pixels, while the second one is adopt after iterations to ultimately interpolate the remaining irrational pixels. Both filters calculate weights based on spatial distance and color variance. For any pixel p , the weight w_p is defined as follows:

$$w_p = \sum_{q \in W_p} e^{-\left[\frac{\sqrt{(L_p - L_q)^2}}{\alpha^2} + \frac{|C_p - C_q|}{\beta^2}\right]} \quad (6)$$

Here, q denote the pixels that fall within the window W_p centered on p , $\sqrt{(L_p - L_q)^2}$ represents the Euclidean distance between the positions of pixels p and q , $|C_p - C_q|$ stands for the color difference between pixels p and q in the RGB space, and α and β are the corresponding spatial and color coefficients.

Additionally, the window sizes w_A and w_B of the two filters W_A and W_B mentioned in Fig. 2, are respectively defined as:

$$w_A = \delta \cdot \frac{2^{N_{iter}}}{2^{n_{iter}}}, w_B = \delta \cdot 2^{n_{iter}} \quad (7)$$

where N_{iter} and n_{iter} represent the total number of iterations and the current number of iterations, respectively. The interval sizes I_A and I_B are set as $1/\delta$ times their corresponding window sizes. Hence, the time complexity of the filtering is maintained at $O(\delta^2)$ and remains independent of the number of iteration rounds.

As for the window sizes of the two filters, the window size of W_A decreases exponentially as iterations progress, thereby increasing focus on the local perception field. In contrast, the window size of W_B exponentially grows with each iteration, enabling the propagation of authentic pixels to a greater extent. Hence, in comparison to TAPA-MVS [13], which employs the bilateral weighted median of neighboring pixels, our filters exhibit a more problem-specific focus for refinement and afford greater flexibility for interpolation.

4) *Iteration procedure*: The proposed refinement mainly involves in two distinct iterations, I_{terA} and I_{terB} . In the first iteration I_{terA} , we employ RANSAC and W_A to propagate reliable depth values. RANSAC is initially adopted to planarize each superpixel, which allows each pixel (x, y) to be assigned its correctly-predicted superpixel depths D_{sp} . The filter W_A is subsequently utilized to further propagate these reliable depths, leveraging the local consistency of superpixels while also preserving the specific details of individual pixels.

Specifically, given the discussions in Section IV-A2, where we found disparity thresholds to be more suitable for evaluation than depth thresholds, we convert the propagated depth d to disparity dp using the following equation:

$$dp = -\frac{1}{\vec{n}_z} (d + \vec{n}_x x + \vec{n}_y y) \quad (8)$$

where $d = -\vec{n}^T [x, y, dp]^T$ denotes the distance to the camera origin, and \vec{n} represents the normal vector of the pixel. Then after converting the depth to disparity, we retain the pixels that satisfy the following condition:

$$|dp^{est} - dp^{org}| < \frac{\mu}{n_{aggr} \times N_{iter}} \quad (9)$$

where dp^{est} and dp^{org} represent the refined disparity gained from depth D_{wa} through Eq. 8 and the initial disparity calculated after PatchMatch Stereo (PMS), respectively. Meanwhile, n_{aggr} represents the aggregated cost in IV-A3 and N_{iter} represents the current iteration round. Pixels whose depth values satisfy the Eq. 9 are deemed trustworthy, and thus, serve as the new input for the ensuing iteration within I_{terA} , while others are provisionally discarded. Successive refinement rounds gradually enhance the reliability of depth predictions, both for individual pixels and their superpixels.

Upon the initial iteration reaches termination, the second iteration I_{terB} is subsequently performed. This procedure constantly employs another WMF, W_B , to interpolate the depth of the residual irrational pixels by referencing the depth values of adjacent reliable pixels. Ultimately, through this

dual-phase iterative processes, we can achieve the refinement and interpolation of erroneous estimates via their adjacent trustworthy pixels.

C. Textureless-aware Segmentation

After iterative correlation refinement, most superpixels in areas with strong texture can accurately perform plane prediction and restore the depth of their internal pixels. However, due to the dearth of high-frequency features during the matching process, pixels in large textureless areas are almost unattainable for reconstruction, as their superpixel predictions tend to deviate.

To better reconstruct large textureless areas, we propose a textureless-aware segmentation method beyond superpixel segmentation as depicted in Fig. 5. Our strategy commences by utilizing Roberts edge detection to extract edges in reference images. Acknowledging that Roberts edge detection occasionally fails to discern certain partial edges, we further employ Hough line detection. Finally, we utilize the two-pass labeling algorithm [48] to merge pixels into distinct regions.

1) *Roberts Edge Detection*: RGB edges in an image represent significant changes in the color gradient. In textureless areas, there is minimal variation in color gradient information, yet edges might still exhibit subtle changes. For instance, objects within a scene may have a uniform base color, but different planes of these objects could interact with lighting in various ways, leading to nuanced color variations. Our objective is to distinguish these planes effectively.

To handle such subtle changes in color gradients, we require an edge detection algorithm with high sensitivity to minor gradient variations. Hence, we opted for the Roberts edge detection algorithm. Compared to the Canny, Sobel, and Laplacian operators, the Roberts operator is recognized for its heightened sensitivity to texture changes and its ability to capture slight color gradient variations, thereby marking it as an optimal choice for our target.

Specifically, for each pixel (x, y) in the reference images I_{ref} , the gradient $g(x, y)$ of grayscale $f(x, y)$ can be computed as follows:

$$g(x, y) = \left(\sqrt{f(x, y)} - \sqrt{f(x+1, y+1)} \right)^2 + \left(\sqrt{f(x+1, y)} - \sqrt{f(x, y+1)} \right)^2 \quad (10)$$

We identify pixels whose gradient exceeding a certain threshold 4 as edges. This technique forms an integral part of our strategy to distinguish planes within textureless areas based on subtle color gradient changes.

2) *Hough Line Detection*: It can be observed that textureless areas, often found in scenarios like walls and floors, typically exhibit regular shapes. To capture these regularities more accurately, we employ the Hough line detection algorithm to complement any discontinuous edges potentially overlooked by the Roberts operator. As shown in Fig. 5, other line detection algorithms like the Line Segment Detector (LSD) primarily focuses on redundant short-edge connections, while the Hough line detection places greater emphasis on long-edge

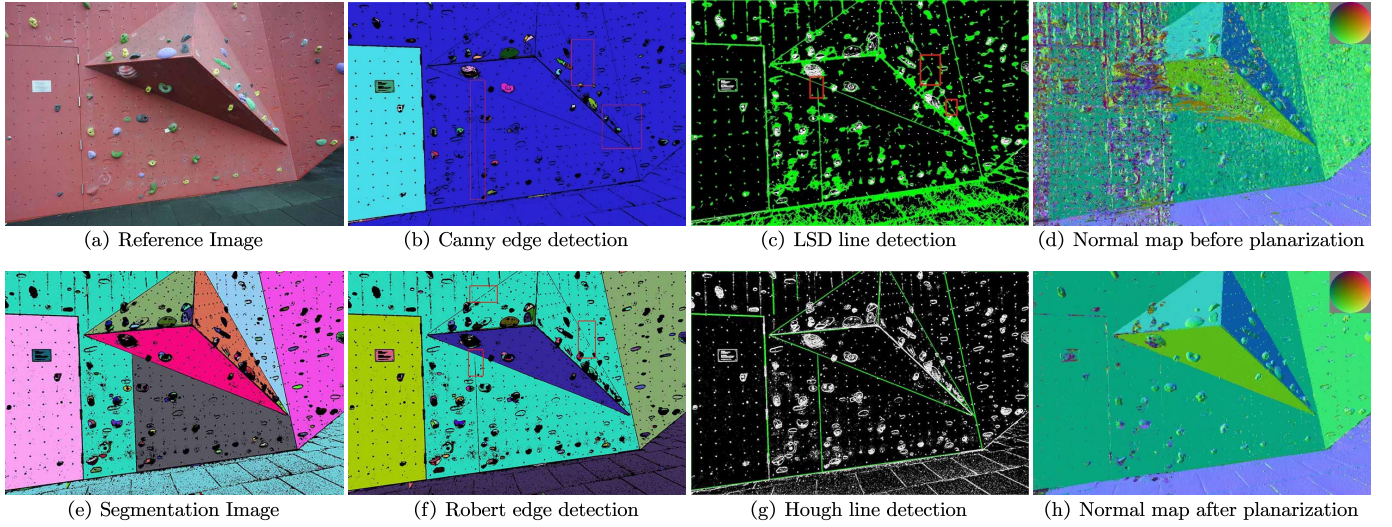


Fig. 5. Textureless-aware segmentation. Note that red boxes in (b), (c) and (f) contain edges that remain undetected and green segments present in (c) and (g) represents detected lines. Additionally, diverse color palettes within (b), (e), and (f) signify distinctively detected planes. Comparing (b) and (f), it is apparent that the Robert detection outperforms the Canny detection in terms of extracting more edges, thereby facilitating plane segmentation. Comparing (c) and (g), it is evident that the Hough detection can successfully connect fractured edges which are missing within red boxes in (f), while the LSD fails to distinguish these necessary edges and introduces redundant connections. Consequently, we opt for the Robert detection and the Hough detection to yield our composite segmentation image in (e) which can successfully differentiate diverse planes. Comparing (d) and (h), it is noteworthy that the textureless-aware segmentation can not only accomplish planarization of textureless areas but also preserve fine details.

connections that are significant for us, thus proving to be more suitable for integration with Robert operator. This combination strategy enables us to circumvent the misclassification of distinct planes as the same caused by color similarities.

The Hough transform is a technique for feature extraction employed in image analysis and digital image processing. Its primary use lies in detecting simple geometric forms like lines. In our work, the Hough transform facilitates the identification of lines corresponding to object edges within textureless areas. More technical details can be found in [49].

Mathematically, the Hough transform works by mapping each point (x, y) in the Cartesian coordinate system into a line $l = -xk + y$ in Hough space. By converting all pixels $(X, Y) = \{(x_i, y_i) \mid i = 1 \cdots N\}$ into lines in Hough space $\mathcal{L} = \{l_i = -x_i k + y_i \mid i = 1 \cdots N\}$, we can then identify intersection points $(L, K) = \{(l_j, k_j) \mid (l_j, k_j) \in l_{a,b,c,\dots}, n_l > \varepsilon\}$, where n_l denotes the number of intersecting lines for each intersection point (l_j, k_j) . These intersection points represent parameters of lines in the original image space and are key to detecting the linear structure within textureless areas.

Note that to adapt our algorithm to the specific traits of diverse image areas, we apply variable maximum connection thresholds, contingent on the segment length. Practically, we observe that longer segments are more tolerant of larger blank intervals, enabling us to effectively handle a wider spectrum of scenarios.

3) *Textureless Area Segmentation*: Specifically, for each image, we first remove lines and edges identified through the application of the Roberts edge detection and Hough line detection algorithms. The remaining points are then grouped into regions based on their connectivity, operating under the assumption that all points within a single region belong to the same plane.

To actualize this, we utilize a two-pass connected component labelling algorithm [48], which aggregates all connected pixels into a region and assigns a unique label to each region. Consequently, the image is divided into several distinct regions $\mathcal{R} = \{R_i \mid i = 1 \cdots M\}$, with each perceived as an individual plane. Regions satisfying the following condition are categorized as textureless areas:

$$R_t \in \{R_j \mid N_j > \kappa \cdot 10^4, j = 1, 2, \dots, M\} \quad (11)$$

In this equation, $\mathcal{N} = \{N_i \mid i = 1 \cdots M\}$ symbolizes the count of pixels within each region. Therefore, we choose regions that encompass a adequate number of pixels. Subsequently, we employ the RANSAC algorithm for planarization and the least square algorithm for refinement.

In order to prevent the erroneous planarization of selected textureless areas, we compare the depth difference between the edge of each textureless plane d_p and its surrounding exteriors neighbors d_n . A subsequent computation of the mean value \bar{D} is served to provide an aggregate measure of the depth differential. Specifically, we calculate \bar{D} as follows:

$$\bar{D} = \frac{1}{N_{edge}} \sum_{p \in P_{edge}} |d_p - d_n| \quad (12)$$

Here, P_{edge} represents the set of points at the edge of each textureless areas, N_{edge} is the total number of these points. We deem the planarization of the textureless area as correct if \bar{D} is less than γ ; otherwise, we won't perform planarization on the erroneously identified plane. This verification step is critical as it prevent the reconstruction of erroneously determined planes.

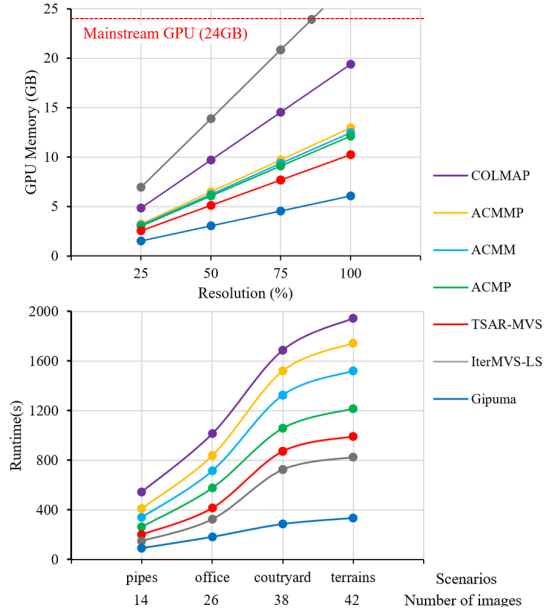


Fig. 6. Total runtime (second) and GPU memory overhead (GB) between different methods before fusion on ETH3D datasets. When comparing the runtime, we select partial scenarios from the ETH3D dataset (*pipes*, *office*, *courtyard* and *terrains*) and scale their image resolution down to 50%. Conversely, when evaluating memory consumption, we align the number of source images to 10 across all method and scale their image into different resolution.

V. FUSION

Given the presence of noise and outliers in the depth maps of individual images, we employ a fusion step to obtain a point cloud result, following the conventional PatchMatch pipeline from [42], [34], which includes a depth and normal consistency check. Specifically, we successively treat each image as a reference and convert its depth map into 3D points in world coordinates. These points are subsequently projected onto neighboring images to get corresponding matches. We consider a match is consistent if it satisfies the following criteria: a relative depth difference less than 0.01, an angle difference between normals less than 30, and a reprojection error of $\Psi \leq 2$, as in [34]. If the number of consistent matches across the neighboring views exceeds 1, the average depth estimate is accepted. Ultimately, the corresponding 3D points and normal estimates of these consistent depth estimations are aggregated and averaged into a unified 3D point.

VI. EXPERIMENT

Our method is evaluated on two prominent MVS datasets, the ETH3D high-resolution multi-view stereo benchmark [25] and the Strecha dataset [26]. Both the ETH3D benchmark and the Strecha dataset are categorized to the datasets with unstructured viewpoints. To validate our design choices, we initially present a series of ablation studies on depth map. Following this, we conducted a qualitative and quantitative evaluation of our point cloud results against various baselines. The experimental results demonstrate that our approach not only significantly outperform most traditional and learning-based methods but also exhibits competitive performance compared with most method.

TABLE I
ACCURACY, COMPLETENESS AND f -score OF POINT CLOUDS WITH MAXIMUM DISTANCE TOLERANCE OF 2cm AND 10cm ON ETH3D TESTING DATASETS. THE BEST RESULTS ARE MARKED IN BOLD WHILE THE SECOND-BEST RESULTS ARE MARKED IN RED.

	method	2cm			10cm		
		Acc.	Com.	f -score	Acc.	Com.	f -score
indoor	COLMAP	91.95	59.65	70.41	98.11	82.82	89.28
	OpenMVS	82	75.92	78.33	95.2	88.84	91.68
	TAPA-MVS	84.83	73.53	77.94	94.23	89.05	91.22
	IterMVS-LS	84.98	75.18	79.38	97.29	87.44	91.94
	Vis-MVSNet	86.58	79.98	82.8	98.34	91.85	94.81
	ACMM	90.99	72.73	79.84	97.79	88.22	92.5
	ACMP	90.6	74.23	80.57	97.1	88.24	92.14
	ACMMP	91.87	80.67	85.39	97.75	94.3	95.93
	TSAR-MVS (Ours)	82.69	88.37	85.33	96.12	96.91	96.49
outdoor	COLMAP	92.04	72.98	80.81	98.64	89.7	93.79
	OpenMVS	81.93	86.41	84.09	96.32	96.48	96.4
	TAPA-MVS	88.37	79.17	82.79	97.04	94.25	95.56
	IterMVS-LS	83.96	80.43	82.11	95.79	91.04	93.34
	Vis-MVSNet	87.72	83.74	85.43	98.07	95.03	96.51
	ACMM	89.63	79.17	83.58	98.85	90.43	94.35
	ACMP	90.35	79.62	84.36	98.55	90.12	94.05
	ACMMP	92.03	83.93	87.38	98.93	95.79	97.28
	TSAR-MVS (Ours)	87.72	86.7	86.84	97.49	97.07	97.27
all	COLMAP	91.97	62.98	73.01	98.25	84.54	90.4
	OpenMVS	81.98	78.54	79.77	95.48	90.75	92.86
	TAPA-MVS	85.71	74.94	79.15	94.93	90.35	92.3
	IterMVS-LS	84.73	76.49	80.06	96.92	88.34	92.29
	Vis-MVSNet	86.86	80.92	83.46	98.27	92.64	95.23
	ACMM	90.65	74.34	80.78	98.05	88.77	92.96
	ACMP	90.54	75.58	81.51	97.47	88.71	92.62
	ACMMP	91.91	81.49	85.89	98.05	94.67	96.27
	TSAR-MVS (Ours)	83.95	87.96	85.71	96.47	96.95	96.69

TABLE II
ACCURACY, COMPLETENESS AND f -score OF POINT CLOUDS WITH MAXIMUM DISTANCE TOLERANCE OF 2cm AND 10cm ON PARTIAL SCENES OF STRECHA DATASETS (*fountain* AND *herzJesu*). THE BEST RESULTS ARE MARKED IN BOLD WHILE THE SECOND-BEST RESULTS ARE MARKED IN RED.

	method	2cm			10cm		
		Acc.	Com.	f -score	Acc.	Com.	f -score
Fountain	COLMAP	89.74	55.87	68.87	98.91	73.73	84.48
	OpenMVS	79.62	70.47	74.77	91.63	83.49	87.37
	IterMVS-LS	83.02	69.45	75.63	93.65	82.61	87.78
	ACMM	85.89	67.32	75.48	94.23	81.29	87.28
	ACMP	86.26	68.53	76.38	94.55	82.15	87.91
	ACMMP	88.53	73.75	80.47	96.18	84.36	89.88
	TSAR-MVS (Ours)	82.27	78.32	80.25	93.34	87.32	90.23
HerzJesu	COLMAP	85.21	46.14	59.86	97.34	55.63	70.8
	OpenMVS	79.76	61.85	69.67	92.53	70.37	79.94
	IterMVS-LS	82.97	60.14	69.73	94.55	69.83	80.33
	ACMM	83.78	57.56	68.24	94.86	67.85	79.11
	ACMP	84.35	59.73	69.94	95.19	69.72	80.49
	ACMMP	86.38	63.41	73.13	96.81	72.65	83.01
	TSAR-MVS (Ours)	82.27	66.82	73.74	94.3	74.69	83.36

A. Dataset and Settings

The ETH3D high-resolution multi-view stereo benchmark [25] comprises 25 scenarios, each includes images of $6,221 \times 4,146$ resolution. Its varying discrete viewpoints and wide variety of scene types pose greater challenges for reconstruction. This dataset is divided into training and testing datasets. The training datasets with 13 scenarios publishes both ground truth point clouds and ground truth depth maps, while the ground truth for the testing set with 12 scenarios is retained by its benchmark site.

The Strecha dataset [26] contains six outdoor scenes. Among these, the Fountain and HerzJesu scenes provide ground truth point clouds, each comprised of 11 and 8 images respectively, with a resolution of $3,072 \times 2,048$.

In order to achieve faster inference times during the actual experiments, we downsampled the images to half of the



Fig. 7. Visualized point cloud results between different methods on partial scenes of ETH3D datasets (*pipes*, *old computer*, *kicker* and *terrains*). TSAR-MVS can effectively reconstruct textureless areas such as floors and walls without detail distortion.

original resolution in both the ETH3D benchmark and the Strecha dataset. This practical adaptation does not compromise the robustness of our approach while enhancing its efficiency.

Our method is implemented on a system equipped with an Intel(R) Core(TM) i7-10700 CPU @ 2.90GHz and an NVIDIA GeForce RTX 3080 graphics card. In joint hypothesis filter, $\{\eta, \tau\} = \{0.8, 0.7\}$. In iterative correlation refinement, $\{\sigma, \alpha, \beta, \delta, \mu\} = \{0.3, 2, 3, 5, 24\}$. In textureless-aware segmentation, $\{\varepsilon, \kappa, \gamma\} = \{5, 0.8, 0.1\}$. Note that we employ a sparse matching strategy that uses every other row and column to speed up the process of the computation of bilateral weighted NCC [34].

B. Point Cloud Evaluation

To evaluate our method, we compare the accuracy (Acc.), completeness (Comp.), and f -score of the produced point clouds with those generated by COLMAP [34], OpenMVS [50], TAPA-MVS [13], IterMVS-LS [19], ACMM [11], ACMP [12], ACMMP [15], and TSAR-MVS. We present quantitative results of the ETH3D benchmark and the Strecha dataset respectively in Tab. I and Tab. II. Note that since the ETH3D dataset provides a benchmark, we directly copied the quantitative results of other baselines from the official website. However, since Strecha only provides point cloud ground truth, we achieved the quantitative results of other baselines by

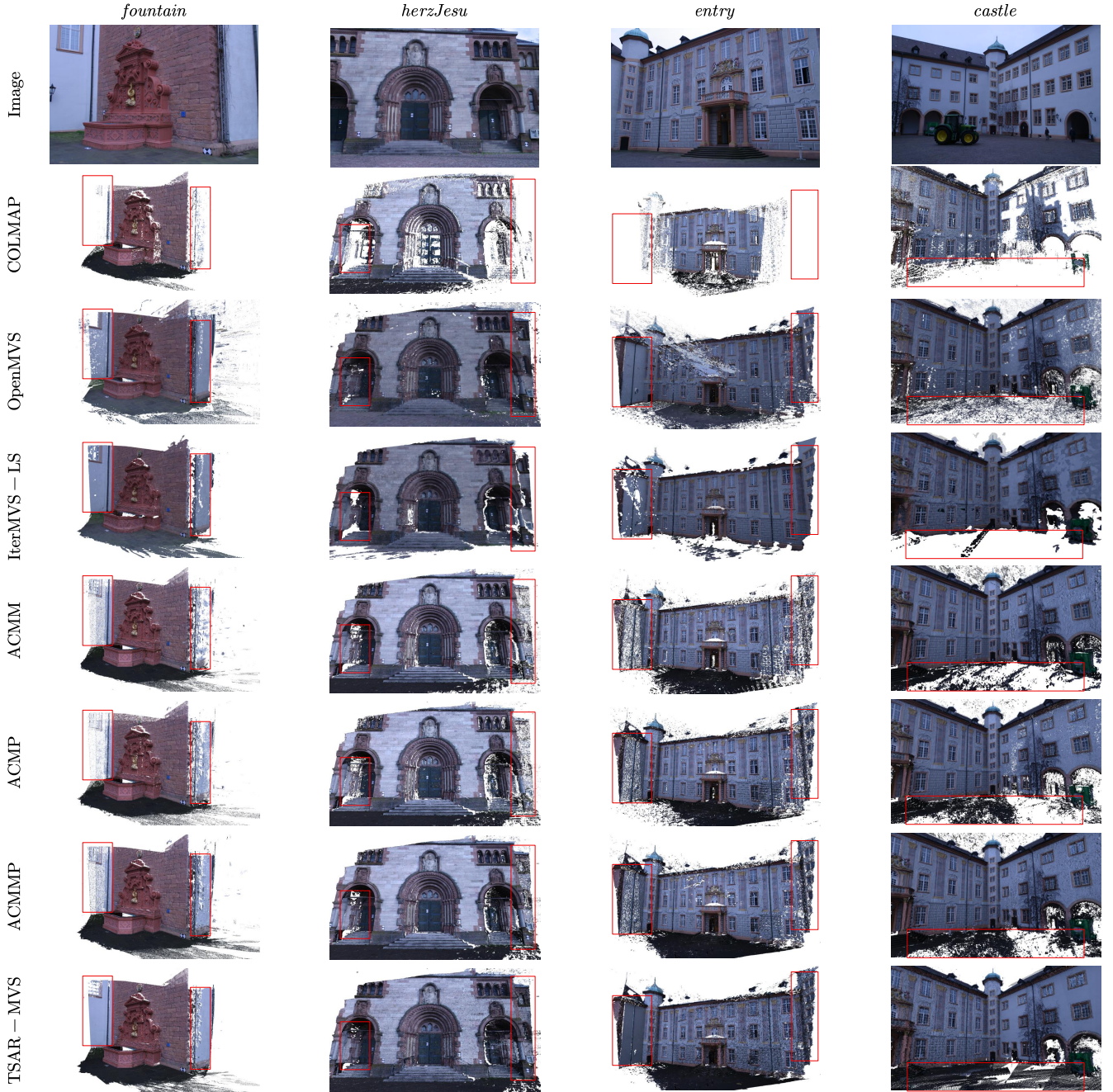


Fig. 8. Visualized point cloud results between different methods on partial scenes of Strecha datasets (*fountain*, *herzJesu*, *entry* and *castle*).

replicating them on our own.

During our evaluation utilizing the ETH3D benchmark, our TSAR-MVS method emerges prominently by securing the highest results in terms of completeness, while also ranking among the foremost for the *f-score*. Even though there are cases where our method trails modestly behind the current state-of-the-art approach, ACMMP, the marginal difference is practically negligible. Turning to the results yielded from the Strecha dataset, our TSAR-MVS method distinctly surpasses other approaches, manifesting superiority in both completeness and overall quality metrics, indicating the resilient competitiveness inherent in our approach and its capacity to match

stride with the most advanced solutions.

Qualitative results of the ETH3D benchmark and the Strecha dataset are respectively illustrated in Fig. 7 and Fig. 8. It is clear that our method yields the most comprehensive results, especially in textureless planar areas like floors and walls, without inducing any conspicuous detail distortion. This observation demonstrates the effectiveness of our method in handling areas that pose challenges for point cloud reconstruction. More results are available in our supplementary materials.

It's also worth noting that our method offers a significant advantage in terms of computational efficiency. Fig. 6 presents the runtime and GPU memory overhead between different

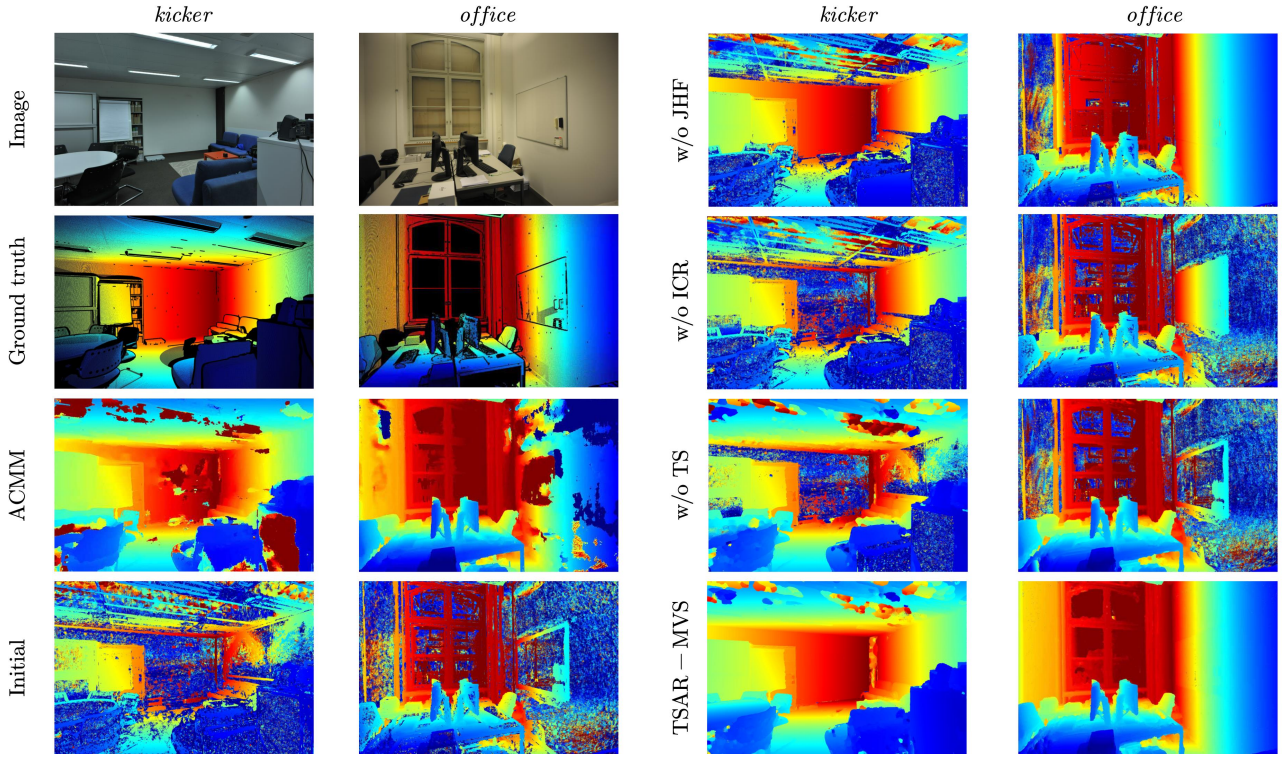


Fig. 9. Visualized depth maps by various ablation methods on partial scenes of ETH3D datasets (*kicker* and *office*). Where the heat value is higher, the larger its depth would be, and vice versa. Black areas in (b) have no ground truth data. TSAR-MVS shows remarkable strength in reconstructing textureless areas.

methods. To exclude the influence of unrelated variables, all methods were implemented on the same system, whose hardware configuration is provided in Section VI-A. Despite IterMVS-LS and Gipuma are faster than TSAR-MVS, the GPU memory overhead demanded by IterMVS-LS is three times that of TSAR-MVS, and Gipuma’s reconstruction quality significantly falls short of TSAR-MVS. Furthermore, TSAR-MVS exhibits superior performance in terms of both time and GPU memory overhead compared to COLMAP, ACMM, ACMP, and ACMMP. This proves that our method is not only effective but also highly practical for applications that require both precision and speed.

C. Ablation Study

To validate the design choices in our method, we conduct a series of experiments to corroborate the effectiveness of each constituent component. Tab. III presents the percentage of unduplicated fused pixels with absolute depth errors less than $2cm$ and $10cm$ of 13 scenes in ETH3D training datasets. Here we term unduplicated fused pixels as pixels that can be fused by at least two views without repetition and adopt the average percentage among all images as quantitative result.

In Tab. III, row 1 presents the results derived from the initial depth map produced by our baseline PatchMatch stereo, which introduces bilateral weighted NCC and adaptive propagation [11] to the original framework. Rows 3-5 respectively display the results when the entire Joint Hypothesis Filtering module is omitted (w/o JHF), only the Disparity Discontinuity component is deleted (w/o DD), and solely the Confidence Estimator component is taken out (w/o CE). Rows 6-8 respectively

illustrate the results when the entire Iterative Correlation Refinement module is excluded (w/o ICR), only the Superpixel Planarization component is removed (w/o SP), and just the WMF component is discarded (w/o WMF). Row 9 showcases the results when the Textureless-aware Segmentation module is erased (w/o TAS). Finally, Row 10 provides the outcomes derived from our complete pipeline.

It is evident that each component of our method contributes significantly to the pipeline, and that each component performs better than ACMM. Specifically, the w/o ICR is worse than w/o JHF and w/o TS, especially in scenes with a higher proportion of textureless areas such as *pipes* and *office*. Hence ICR module contributes more to the reconstruction results than JHF and TS, which further emphasizing the significance of the ICR module that spreads the reliable depth of pixels to the adjacent ones. Moreover, although w/o JHF and w/o TS achieve similar average percentage, their performance diverges across different scenes. Specifically, w/o JHF outperforms w/o TS in scenarios with more textureless areas such as *pipes* and *office*, since TS is targeted towards handling textureless textures, whereas JHF is beneficial for the restoration of fine details. This observation is further substantiated in Fig. 9 and supplementary materials.

In the joint hypothesis filter, the performance of w/o DD essentially aligns with that of w/o CE, suggesting that both disparity continuity filtering and the confidence estimator respectively contribute similar enhancements from different perspectives of disparity and cost. In iterative correlation refinement, the performance of w/o WMF slightly surpasses that of w/o SP. This indicates that compared to the final

TABLE III
PERCENTAGE OF UNDUPLICATED FUSED PIXELS WITH MAXIMUM DEPTH TOLERANCE OF 2cm AND 10cm ON ETH3D TRAINING DATASETS.
UNDUPLICATED FUSED PIXELS MAY AVOID THE IMPACT OF ERRONEOUS RECONSTRUCTION WITHIN SINGLE PERSPECTIVE.

error	method	Ave.	indoor							outdoor					
			delive.	kicker	office	pipes	relief	relief_2	terrace	courty.	electro	faade	meadow	playgr.	terrace
2cm	PMS Prior	21.99	19.47	22.55	17.23	22.97	27.51	26.78	23.04	22.41	29.05	19.29	14.67	17.62	23.3
	ACMM	32.58	27.64	32.6	29.13	37.09	38.63	35.45	29.58	33.59	40.26	26.34	35.43	26.43	31.43
	w/o JHF	41.45	35.93	31.49	29.96	45.57	44.26	46.95	50.36	46.41	53.73	34.07	23.27	46.63	50.16
	w/o DD	41.98	36.99	31.9	32.08	45.93	44.03	46.77	50.97	46.69	54.26	34.13	24.65	46.85	50.43
	w/o CE	42.19	36.37	32.12	34.36	45.77	44.1	46.76	51.23	46.88	54.51	34.25	24.73	47.12	50.27
	w/o ICR	36.76	33.28	24.64	18.31	31.53	41.97	43.83	47.88	45.23	52.32	32.99	15.91	41.91	48.09
	w/o SP	39.42	34.53	28.14	27.4	37.82	42.64	44.63	49.35	46.27	53.18	33.46	22.48	43.84	48.76
	w/o WMF	40.87	35.26	30.52	33.65	41.27	42.78	44.85	49.12	46.82	53.98	33.71	25.35	44.37	49.57
	w/o TS	40.15	34.38	28.34	25.86	42.31	44.58	47.31	52.1	47.18	53.25	33.41	20.12	43.68	49.37
	TSAR-MVS	44.76	37.34	35.71	44.76	46.54	44.82	47.52	53.33	48.4	55.15	34.98	33.28	48.95	51.11
10cm	PMS Prior	24.67	21.01	26.47	20.35	27.67	27.93	27.27	24.51	26.14	32.29	24.89	17.69	19.92	24.59
	ACMM	37.11	33.91	39.21	34.55	39.6	39.66	36.54	31.84	37.95	45.21	35.2	42.07	30.45	36.19
	w/o JHF	48.78	42.93	38.64	35.03	50.73	47.33	49.77	57.85	53.57	61.17	48.93	36.1	53.64	58.45
	w/o DD	49.31	44.16	39.08	36.94	51.53	46.97	49.6	58.04	53.85	61.44	48.93	37.96	53.91	58.61
	w/o CE	49.52	43.34	39.2	39.46	51.46	47.05	49.68	58.12	54.03	61.6	48.94	38.12	54.18	58.55
	w/o ICR	43.38	38.64	28.89	25.66	35.77	44.02	46.48	54.41	52	58.83	46.85	28.23	48.33	55.81
	w/o SP	46.30	40.52	34.18	34.39	41.48	44.86	47.42	55.89	53.21	59.74	47.54	35.37	50.63	56.65
	w/o WMF	47.88	41.73	37.42	40.71	45.05	45.07	47.67	55.63	53.87	60.57	47.83	38.06	51.34	57.53
	w/o TS	47.14	40.18	35.23	31.42	47.82	47.45	50.37	55.44	54.78	59.49	48.34	33.18	51.9	57.17
	TSAR-MVS	52.40	45.52	43.14	52.56	52.17	47.58	50.51	58.6	56.1	62.14	49.98	47.3	56.25	59.32

TABLE IV
ACCURACY, COMPLETENESS AND *f-score* OF POINT CLOUDS WITH MAXIMUM DISTANCE TOLERANCE OF 2cm AND 10cm ON ETH3D TRAINING DATASETS. THE BEST RESULTS ARE MARKED IN BOLD WHILE THE SECOND-BEST RESULTS ARE MARKED IN RED.

	method	2cm			10cm		
		Acc.	Com.	<i>f-score</i>	Acc.	Com.	<i>f-score</i>
indoor	Gipuma	89.25	24.61	35.8	98.15	42.62	56.17
	Gipuma + TSAR-MVS	78.67	44.18	55.27	93.61	65.37	75.34
	COLMAP	95.01	52.90	66.76	98.82	76.90	86.03
	COLMAP + TSAR-MVS	88.36	76.86	81.64	95.94	89.64	92.31
	ACMM	92.46	68.49	78.13	97.71	84.64	90.43
	ACMM + TSAR-MVS	92.11	85.84	88.81	97.79	97.02	97.39
	TSAR-MVS	87.41	85.98	86.58	97.33	96.60	96.95
outdoor	Gipuma	83.23	25.26	37.07	98.76	45.5	61.27
	Gipuma + TSAR-MVS	74.57	49.27	58.46	92.36	71.53	79.12
	COLMAP	88.16	57.73	68.70	98.66	82.46	89.46
	COLMAP + TSAR-MVS	82.19	68.71	74.48	96.18	89.53	92.47
	ACMM	88.57	72.67	79.71	98.59	88.46	93.19
	ACMM + TSAR-MVS	85.67	76.63	80.77	97.26	92.61	94.78
	TSAR-MVS	82.89	77.94	80.32	97.18	92.25	94.60
all	Gipuma	86.47	24.91	36.38	98.43	43.95	58.52
	Gipuma + TSAR-MVS	76.78	46.53	56.74	93.03	68.21	77.08
	COLMAP	91.85	55.13	67.66	98.75	79.47	87.61
	COLMAP + TSAR-MVS	85.51	73.09	78.34	96.05	89.59	92.39
	ACMM	90.67	70.42	78.86	98.12	86.40	91.70
	ACMM + TSAR-MVS	89.14	81.59	85.10	97.54	94.99	96.19
	TSAR-MVS	85.32	82.27	83.69	97.26	94.59	95.86

interpolation of erroneous pixels, the propagation of effective pixels through superpixels planarization proves to be more crucial.

Fig. 9 offers a visual representation of the results. We also provide depth images displayed in pseudo colors for a more intuitive comparison. Clearly, TSAR-MVS yields the most complete depth map, particularly in textureless areas, which often present challenges in reconstruction. As shown, w/o JHF erroneously estimates partial superpixels due to the absence of filtering, leading to severe deviations in the planarization of textureless areas. On the other hand, w/o ICR, which lacks superpixel prediction, not only distorts details in well-textured areas but also causes shifts in the reconstruction of textureless areas. Moreover, due to the absence of textureless-aware segmentation, w/o TS falls short in scenes with a large number of textureless areas. However, TSAR-MVS produces

the most realistic results, avoiding both plane shifting and detail distortion.

Moreover, to demonstrate the universality of our TSAR-MVS approach, we conducted a series of experiments wherein we substitute the depth prior from baseline PatchMatch stereo into other methods, including Gipuma [42], COLMAP [34] and ACMM [11], as shown in Tab. IV. We adopt the modified version of Gipuma as prior of our method rather than Gipuma or ACMM is to pursue high-quality reconstruction while striving for temporal efficiency. While Gipuma excels in speed, its reconstruction results leave much to be desired. ACMM might serve as a superior prior in terms of results, but its multi-scale framework tends to be time-consuming. Hence, by incorporating bilateral weighted NCC and adaptive propagation from ACMM into Gipuma, we can ensure both speed and the provision of excellent depth priors for reconstruction, creating a beneficial blend of both models.

As indicated by the results presented in Table III, the integration of our method with each of these initial depth inputs engenders noticeable improvements. Comparatively, the results achieved through COLMAP demonstrated a greater refinement than those acquired using ACMM. This suggests that our method yields more significant enhancements when faced with an unreliable initial depth. Given that ACMM exhibits superior performance than COLMAP in addressing textureless area challenges, it further validates that our method is especially proficient at refining depth when initial readings in textureless zones are flawed. These findings collectively corroborate the potential of our TSAR-MVS to be effectively applied across a range of techniques, thereby reaffirming its universal adaptability.

VII. CONCLUSION

In this paper, we introduced TSAR-MVS, a novel multi-view stereo method explicitly designed for the reconstruction of textureless areas. First, we present joint hypothesis filtering,

a synergistic blend of a confidence estimator and disparity discontinuity filtering, thus enabling us to provisionally discard erroneous estimates. Subsequently, We implement iterative correlation refinement, utilizing RANSAC and WMF to iteratively fill in areas with robust hypotheses derived from nearby trustworthy regions. Moreover, we propose textureless-aware segmentation, a distinctive fusion of edge and line detection techniques, functioning as a flexible mechanism that enables adaptive recognition of textureless regions.

Experiments on the high-resolution ETH3D multi-view benchmark and the Strecha dataset have demonstrated that our framework can provide smooth estimations of planar regions and accurately reconstruct 3D scenes. We also conducted a series of empirical experiments to validate the rationale behind each component of our approach, and to demonstrate the wide applicability of TSAR-MVS. In the future, we look forward to further refining our approach and exploring its potential applications in a broader range of scenarios.

REFERENCES

- [1] A. Kuhn, H. Hirschmüller, D. Scharstein, and H. Mayer, “A TV prior for high-quality scalable multi-view stereo reconstruction,” *Int. J. Comput. Vis.*, vol. 124, pp. 2–17, 2017.
- [2] S. Shen, “Accurate multiple view 3d reconstruction using patch-based stereo for large-scale scenes,” *IEEE Trans. Image Process.*, vol. 22, no. 5, pp. 1901–1914, 2013.
- [3] Q. Shan, B. Curless, Y. Furukawa, C. Hernandez, and S. M. Seitz, “Occluding contours for multi-view stereo,” in *Proc. IEEE/CVF Conf. Comput. Vis. Pattern Recognit. (CVPR)*, June 2014.
- [4] E. Zheng, E. Dunn, V. Jovic, and J. Frahm, “Patchmatch based joint view selection and depthmap estimation,” in *Proc. IEEE/CVF Conf. Comput. Vis. Pattern Recognit. (CVPR)*, June 2014, pp. 1510–1517.
- [5] Y. Furukawa and J. Ponce, “Accurate, dense, and robust multiview stereopsis,” *IEEE Trans. Pattern Anal. Mach. Intell.*, vol. 32, no. 8, pp. 1362–1376, 2010.
- [6] Y. Yao, Z. Luo, S. Li, T. Fang, and L. Quan, “Mvsnet: Depth inference for unstructured multi-view stereo,” in *Proc. Eur. Conf. Comput. Vis. (ECCV)*, September 2018.
- [7] K. Luo, T. Guan, L. Ju, H. Huang, and Y. Luo, “P-mvsnet: Learning patch-wise matching confidence aggregation for multi-view stereo,” in *Proc. IEEE/CVF Int. Conf. Comput. Vis. (ICCV)*, 2019, pp. 10451–10460.
- [8] J. Y. Lee, J. DeGol, C. Zou, and D. Hoiem, “Patchmatch-rl: Deep mvs with pixelwise depth, normal, and visibility,” in *Proc. IEEE/CVF Int. Conf. Comput. Vis. (ICCV)*, October 2021, pp. 6158–6167.
- [9] P. Heise, S. Klose, B. Jensen, and A. Knoll, “Pm-huber: Patchmatch with huber regularization for stereo matching,” in *Proc. IEEE/CVF Int. Conf. Comput. Vis. (ICCV)*, December 2013.
- [10] A. Kuhn, S. Lin, and O. Erdler, “Plane completion and filtering for multi-view stereo reconstruction,” in *Pattern Recognition*, 2019, pp. 18–32.
- [11] Q. Xu and W. Tao, “Multi-scale geometric consistency guided multi-view stereo,” in *Proc. IEEE/CVF Conf. Comput. Vis. Pattern Recognit. (CVPR)*, June 2019.
- [12] —, “Planar prior assisted patchmatch multi-view stereo,” *Proc. of the AAAI Conf. Artif. Intell. (AAAI)*, vol. 34, no. 07, pp. 12516–12523, 2020.
- [13] A. Romanoni and M. Matteucci, “Tapa-mvs: Textureless-aware patchmatch multi-view stereo,” in *Proc. IEEE/CVF Int. Conf. Comput. Vis. (ICCV)*, 2019.
- [14] F. Wang, S. Galliani, C. Vogel, P. Speciale, and M. Pollefeys, “Patchmatchnet: Learned multi-view patchmatch stereo,” in *Proc. IEEE/CVF Conf. Comput. Vis. Pattern Recognit. (CVPR)*, 2021, pp. 14194–14203.
- [15] Q. Xu, W. Kong, W. Tao, and M. Pollefeys, “Multi-Scale Geometric Consistency Guided and Planar Prior Assisted Multi-View Stereo,” *IEEE Trans. Pattern Anal. Mach. Intell.*, pp. 1–18, 2022.
- [16] C. Zhang, Z. Li, Y. Cheng, R. Cai, H. Chao, and Y. Rui, “Meshstereo: A global stereo model with mesh alignment regularization for view interpolation,” in *Proc. IEEE/CVF Int. Conf. Comput. Vis. (ICCV)*, December 2015.
- [17] Y. Wang, Z. Zeng, T. Guan, W. Yang, Z. Chen, W. Liu, L. Xu, and Y. Luo, “Adaptive patch deformation for textureless-resilient multi-view stereo,” in *Proc. IEEE/CVF Conf. Comput. Vis. Pattern Recognit. (CVPR)*, 2023, pp. 1621–1630.
- [18] J. Yang, W. Mao, J. M. Alvarez, and M. Liu, “Cost volume pyramid based depth inference for multi-view stereo,” in *Proc. IEEE/CVF Conf. Comput. Vis. Pattern Recognit. (CVPR)*, 2020, pp. 4876–4885.
- [19] F. Wang, S. Galliani, C. Vogel, and M. Pollefeys, “Itermvs: Iterative probability estimation for efficient multi-view stereo,” in *Proc. IEEE/CVF Conf. Comput. Vis. Pattern Recognit. (CVPR)*, 2022, pp. 8606–8615.
- [20] C. Sormann, E. Santellani, M. Rossi, A. Kuhn, and F. Fraundorfer, “DELS-MVS: deep epipolar line search for multi-view stereo,” in *Proc. IEEE/CVF Winter Conf. Appl. of Comput. Vis. (WACV)*, January 2023, pp. 3086–3095.
- [21] X. Ma, Y. Gong, Q. Wang, J. Huang, L. Chen, and F. Yu, “Epp-mvsnet: Epipolar-assembling based depth prediction for multi-view stereo,” in *Proc. IEEE/CVF Int. Conf. Comput. Vis. (ICCV)*, 2021, pp. 5712–5720.
- [22] Z. Li, W. Zuo, Z. Wang, and L. Zhang, “Confidence-based large-scale dense multi-view stereo,” *IEEE Trans. Image Process.*, vol. 29, pp. 7176–7191, 2020.
- [23] A. Kuhn, C. Sormann, M. Rossi, O. Erdler, and F. Fraundorfer, “Deepc-mvs: Deep confidence prediction for multi-view stereo reconstruction,” in *Int. Conf. 3D Vis. (3DV)*, November 2020, pp. 404–413.
- [24] H. Hirschmüller, “Stereo processing by semiglobal matching and mutual information,” *IEEE Trans. Pattern Anal. Mach. Intell.*, vol. 30, no. 2, pp. 328–341, 2008.
- [25] T. Schops, J. L. Schonberger, S. Galliani, T. Sattler, K. Schindler, M. Pollefeys, and A. Geiger, “A multi-view stereo benchmark with high-resolution images and multi-camera videos,” in *Proc. IEEE/CVF Conf. Comput. Vis. Pattern Recognit. (CVPR)*, July 2017.
- [26] C. Strecha, W. von Hansen, L. Van Gool, P. Fua, and U. Thoennessen, “On benchmarking camera calibration and multi-view stereo for high resolution imagery,” in *Proc. IEEE/CVF Conf. Comput. Vis. Pattern Recognit. (CVPR)*, 2008, pp. 1–8.
- [27] G. Vogiatzis, C. Hernandez Esteban, P. H. Torr, and R. Cipolla, “Multiview stereo via volumetric graph-cuts and occlusion robust photo-consistency,” *IEEE Trans. Pattern Anal. Mach. Intell.*, vol. 29, no. 12, pp. 2241–2246, 2007.
- [28] A. Osman Ulusoy, M. J. Black, and A. Geiger, “Semantic multi-view stereo: Jointly estimating objects and voxels,” in *Proc. IEEE/CVF Conf. Comput. Vis. Pattern Recognit. (CVPR)*, 2017.
- [29] D. Cremers and K. Kolev, “Multiview stereo and silhouette consistency via convex functionals over convex domains,” *IEEE Trans. Pattern Anal. Mach. Intell.*, vol. 33, no. 6, pp. 1161–1174, 2011.
- [30] Z. Li, K. Wang, W. Zuo, D. Meng, and L. Zhang, “Detail-preserving and content-aware variational multi-view stereo reconstruction,” *IEEE Trans. Image Process.*, vol. 25, no. 2, pp. 864–877, 2016.
- [31] A. Locher, M. Perdoch, and L. Van Gool, “Progressive prioritized multi-view stereo,” in *Proc. IEEE/CVF Conf. Comput. Vis. Pattern Recognit. (CVPR)*, 2016.
- [32] M. Goesele, N. Snavely, B. Curless, H. Hoppe, and S. M. Seitz, “Multi-view stereo for community photo collections,” in *Proc. IEEE/CVF Int. Conf. Comput. Vis. (ICCV)*, 2007, pp. 1–8.
- [33] J. L. Schonberger and J.-M. Frahm, “Structure-from-motion revisited,” in *Proc. IEEE/CVF Conf. Comput. Vis. Pattern Recognit. (CVPR)*, 2016.
- [34] J. L. Schönberger, E. Zheng, J.-M. Frahm, and M. Pollefeys, “Pixelwise view selection for unstructured multi-view stereo,” in *Proc. Eur. Conf. Comput. Vis. (ECCV)*, 2016, pp. 501–518.
- [35] Z. Xu, Y. Liu, X. Shi, Y. Wang, and Y. Zheng, “MARMVS: matching ambiguity reduced multiple view stereo for efficient large scale scene reconstruction,” in *Proc. IEEE/CVF Conf. Comput. Vis. Pattern Recognit. (CVPR)*, June 2020, pp. 5980–5989.
- [36] J. Zhang, S. Li, Z. Luo, T. Fang, and Y. Yao, “Vis-mvsnet: Visibility-aware multi-view stereo network,” *Int. J. Comput. Vis. (IJCV)*, pp. 199–214, 2023.
- [37] Z. Mi, D. Chang, and D. Xu, “Generalized binary search network for highly-efficient multi-view stereo,” in *Proc. IEEE/CVF Conf. Comput. Vis. Pattern Recognit. (CVPR)*, June 2022, pp. 12981–12990.
- [38] Y. Yao, Z. Luo, S. Li, T. Shen, T. Fang, and L. Quan, “Recurrent mvsnet for high-resolution multi-view stereo depth inference,” in *Proc. IEEE/CVF Conf. Comput. Vis. Pattern Recognit. (CVPR)*, 2019, pp. 5525–5534.
- [39] Q. Xu and W. Tao, “Pvsnet: Pixelwise visibility-aware multi-view stereo network,” *arXiv:2007.07714[cs.CV]*, July 2007, doi:10.48550/arXiv.2007.07714.

- [40] C. Barnes, E. Shechtman, A. Finkelstein, and D. B. Goldman, "Patch-match: A randomized correspondence algorithm for structural image editing," *ACM Trans. Graph.*, vol. 28, no. 3, p. 24, 2009.
- [41] M. Bleyer, C. Rhemann, and C. Rother, "Patchmatch stereo - stereo matching with slanted support windows," in *British Mach. Vis. Conf. (BMVC)*, J. Hoey, S. J. McKenna, and E. Trucco, Eds., September 2011, pp. 1–11.
- [42] S. Galliani, K. Lasinger, and K. Schindler, "Massively parallel multiview stereopsis by surface normal diffusion," in *Proc. IEEE/CVF Int. Conf. Comput. Vis. (ICCV)*, December 2015.
- [43] R. Gouveia, A. Spyropoulos, and P. Mordohai, "Confidence estimation for superpixel-based stereo matching," in *Int. Conf. 3D Vis. (3DV)*, 2015, pp. 180–188.
- [44] T. Xue, A. Owens, D. Scharstein, M. Goesele, and R. Szeliski, "Multi-frame stereo matching with edges, planes, and superpixels," *Image Vis. Comput.*, vol. 91, 2019.
- [45] W. Jung and J. Han, "Depth map refinement using super-pixel segmentation in multi-view systems," in *Proc. IEEE/CVF Conf. Consumer Elect. (ICCE)*. IEEE, January 2021, pp. 1–5.
- [46] N. Huang, Z. Huang, C. Fu, H. Zhou, Y. Xia, W. Li, X. Xiong, and S. Cai, "A multiview stereo algorithm based on image segmentation guided generation of planar prior for textureless regions of artificial scenes," *IEEE J. Sel. Top. Appl. Earth Obs. Remote. Sens.*, vol. 16, pp. 3676–3696, 2023.
- [47] R. Achanta, A. Shaji, K. Smith, A. Lucchi, P. Fua, and S. Süsstrunk, "Slic superpixels compared to state-of-the-art superpixel methods," *IEEE Trans. Pattern Anal. Mach. Intell.*, vol. 34, no. 11, pp. 2274–2282, 2012.
- [48] K. Wu, E. J. Otoo, and K. Suzuki, "Optimizing two-pass connected-component labeling algorithms," *Pattern Anal. Appl.*, vol. 12, no. 2, pp. 117–135, 2009.
- [49] D. Ballard, "Generalizing the hough transform to detect arbitrary shapes," *Pattern Recognition*, vol. 13, no. 2, pp. 111–122, 1981.
- [50] D. Cernea, "OpenMVS: Multi-View Stereo Reconstruction Library," 2020, Accessed: Nov. 28, 2022. [Online]. Available: <https://cdseacave.github.io/openMVS>